

**Continuous and pulsed selective laser melting of Ti6Al4V lattice structures  
Effect of post-processing on microstructural anisotropy and fatigue behaviour**

Karami, K.; Blok, A.; Weber, L.; Ahmadi, S. M.; Petrov, R.; Nikolic, Ksenija; Borisov, E.V.; Leeflang, S.; Ayas, C.; Zadpoor, A. A.

**DOI**

[10.1016/j.addma.2020.101433](https://doi.org/10.1016/j.addma.2020.101433)

**Publication date**

2020

**Document Version**

Final published version

**Published in**

Additive Manufacturing

**Citation (APA)**

Karami, K., Blok, A., Weber, L., Ahmadi, S. M., Petrov, R., Nikolic, K., Borisov, E. V., Leeflang, S., Ayas, C., Zadpoor, A. A., Mehdipour, M., Reinton, E., & Popovich, V. A. (2020). Continuous and pulsed selective laser melting of Ti6Al4V lattice structures: Effect of post-processing on microstructural anisotropy and fatigue behaviour. *Additive Manufacturing*, 36, Article 101433. <https://doi.org/10.1016/j.addma.2020.101433>

**Important note**

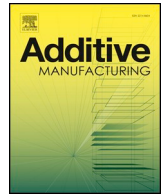
To cite this publication, please use the final published version (if applicable).  
Please check the document version above.

**Copyright**

Other than for strictly personal use, it is not permitted to download, forward or distribute the text or part of it, without the consent of the author(s) and/or copyright holder(s), unless the work is under an open content license such as Creative Commons.

**Takedown policy**

Please contact us and provide details if you believe this document breaches copyrights.  
We will remove access to the work immediately and investigate your claim.



# Continuous and pulsed selective laser melting of Ti6Al4V lattice structures: Effect of post-processing on microstructural anisotropy and fatigue behaviour

K. Karami<sup>a</sup>, A. Blok<sup>a</sup>, L. Weber<sup>a</sup>, S.M. Ahmadi<sup>a,b</sup>, R. Petrov<sup>a,c</sup>, Ksenija Nikolic<sup>c</sup>, E.V. Borisov<sup>d</sup>, S. Leeflang<sup>a</sup>, C. Ayas<sup>a</sup>, A.A. Zadpoor<sup>a</sup>, M. Mehdipour<sup>a</sup>, E. Reinton<sup>a</sup>, V.A. Popovich<sup>a,\*</sup>

<sup>a</sup> Faculty of Mechanical, Maritime, and Materials Engineering, Delft University of Technology (TU Delft), Mekelweg 2, 2628 CD, Delft, the Netherlands

<sup>b</sup> Amber Implants, Delft, the Netherlands

<sup>c</sup> Department of Materials Science and Engineering, Ghent University, Ghent, Belgium

<sup>d</sup> Peter the Great Saint-Petersburg Polytechnic University, Saint Petersburg, Russia

## ARTICLE INFO

### Keywords:

Additive manufacturing  
Ti6Al4V lattice  
Laser scanning strategy  
Post treatment  
Fatigue behaviour

## ABSTRACT

Additive manufacturing technologies in general and laser powder bed fusion (L-PBF) in particular have been on the rise in different applications, including biomedical implants. The effects of the various L-PBF process parameters on the microstructure and properties of Ti6Al4V lattice structures have been studied before. However, the relationship between the different modes of laser scanning and the resulting microstructure, internal imperfections, and surface morphology is still underexplored. In this study, the aforementioned parameters and their effect on the compressive mechanical properties and fatigue behaviour of lattice titanium have been studied for both continuous and pulsed laser scanning modes. Moreover, the influence of various combinations of post-processing treatments, such as hot isostatic pressing (HIP), sandblasting, and chemical etching, on the quasi-static mechanical properties and fatigue endurance of the resulting materials were investigated. It was found that continuous laser strategy results in fewer imperfections and higher fatigue resistance, while pulsed laser showed a more homogenous microstructure; likely leading to a more isotropic behaviour. Furthermore, the continuous mode showed larger prior  $\beta$  grains preferentially oriented in the building direction, while pulsed specimens exhibited finer equiaxed grains with no preferred orientations. The highest level of fatigue life was obtained by using an optimized combination of HIP, sandblasting, and chemical etching.

## 1. Introduction

During recent decades, additive manufacturing (AM) has gradually evolved from a tool for rapid prototyping to a novel manufacturing method [1,2]. According to the joint ISO/ASTM52900 – 15 terminology [3], AM techniques are divided into seven major categories, such as laser powder bed fusion (L-PBF) commonly known as selective laser melting (SLM) or flow-based (directed energy deposition (DED)) techniques [4–8]. In L-PBF, the molten powder is fused and subsequently solidified to form the part sequentially layer by layer under an inert atmosphere [9,10]. L-PBF can be utilized for printing the required parts using different process parameters, such as laser power, hatch distance, scan speed, layer thickness and scanning modes.

For the AM of porous structures two scanning modes can be used, namely Vector-based [14] and the most commonly applied Contour-

and-hatching [11,12]. In the Vector-based scanning mode, which is also called single point exposure or “pulsed laser-based” (PLB) [14], the strut diameter of the lattice structure is not specified, and these slender members are described by vectors. Each intersection point of a vector and a building layer is scanned in a single pulse by a Modulated Continuous Wave (CW) laser beam with a certain power and exposure time [15]. In case of lattice structures higher power and longer exposure will result in a larger melt pool and therefore the strut diameter of the lattice is directly dependent on these process parameters. In the Contour-and-hatching scanning mode, which is also called “continuous laser-based” (CLB), the strut diameter of the lattice structure is predefined by a CAD-design [13]. The original CAD geometry contours are offset (typically by half the melt-pool diameter) and the laser beam subsequently continuously scans the contours and fills the bulk with a pre-selected raster pattern or hatching. The laser parameters for this building strategy have

\* Corresponding author.

E-mail address: [v.popovich@tudelft.nl](mailto:v.popovich@tudelft.nl) (V.A. Popovich).

<https://doi.org/10.1016/j.addma.2020.101433>

Received 28 April 2020; Received in revised form 8 June 2020; Accepted 3 July 2020

Available online 08 July 2020

2214-8604/© 2020 The Author(s). Published by Elsevier B.V. This is an open access article under the CC BY license (<http://creativecommons.org/licenses/by/4.0/>).

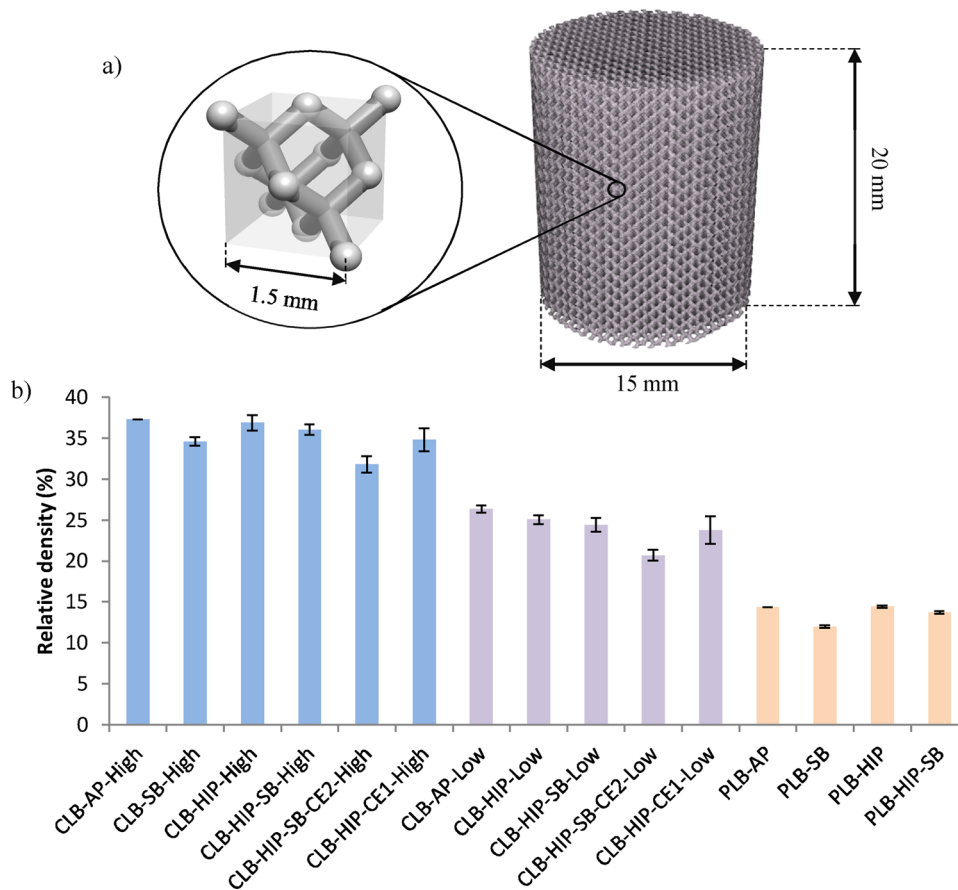


Fig. 1. a) Sample geometry showing cubic diamond cell structure b) the relative density of all sample groups.

**Table 1**

L-PBF process parameters used for Pulsed and Continuous laser-based lattice Ti6Al4V [13,43].

L-PBF scanning strategy	Pulsed laser-based (PLB)	Continuous laser-based (CLB)
L-PBF machine type	SLM 125, Realizer GmbH	SLM Solutions, 280 <sup>HL</sup>
Fibre laser	Single IPG Photonics	twin (2 × 400 W) IPG Photonics
Laser Power, (W)	128	320
Wavelength range, (nm)	1070 ± 10	1070 ± 10
Maximum emitting power, (W)	400	400
Layer thickness, (µm)	50	30
Scan speed, (m/s)	–	10
Exposure time, (µs)	550	–
Powder particle size, (µm)	15 – 45 (grade 23)	20 – 63 (grade 23)

**Table 2**

Chemical composition of Ti6Al4V powder (grade 23) (in mass fraction %).

Element	Ti	Al	V	C	O	N	Fe	H	Other
Min	Balance	5.50	3.50						
Max	Balance	6.50	4.50	0.08	0.13	0.03	0.25	0.0125	0.10

a power, a distance and a time component. These are selected differently, depending on the type of laser used. For a CW laser, the laser parameters are laser power and scanning speed, while for a Modulated CW laser, they are laser power, laser exposure time and point distance. Depending on the combination of the optimized process parameters, different microstructural and mechanical properties can be obtained with these scanning modes.

Titanium and its alloys have been extensively used for biomedical and aerospace applications [16–18] due to their suitable elastic modulus, fracture toughness, fatigue strength with respect to density [19], corrosion resistance, and biocompatibility [20,21]. Ti6Al4V is a titanium alloy, which has been widely used for biomedical implant manufacturing. Implants should be able to mimic the mechanical properties, in particular the elastic modulus of the host bone. The elastic modulus of Ti6Al4V is 115 GPa, whereas that of cortical bone is 7.7–21.8 GPa [22]. Because of this mismatch, the mechanical stress can be taken up by the implant (the stress shielding phenomenon), which will result in bone unloading and, thus, bone resorption that could lead to the loosening of the implant. Therefore, the biomedical applications of Ti6Al4V critically depend on decreasing the elastic modulus of the biomaterial to an appropriate range. The elastic modulus of AM open cellular lattice Ti6Al4V is in the range of the bone [23]. In addition, from the osseointegration point of view, the lattice structure enables tissue ingrowth, body fluid circulation, and cell proliferation [22,24]. Porous or lattice materials (also called meta-biomaterials [25]) present specific

**Table 3**  
The post-processing treatments applied in the current study.

Sub-group (designation)	Post-processing parameters
As-processed (AP)	L-PBF Ti6Al4V with a diamond unit cell of 1.5 mm.
Hot isostatic pressing (HIP)	Heated at 920 °C under 100 MPa pressure for 120 min in an argon atmosphere followed by furnace cooling at a rate of 10 °C/min.
Sand blasting (SB)	Sandblasting with abrasive Al <sub>2</sub> O <sub>3</sub> particles (50 µm) for 90 s with a nozzle pressure of 4.5 bar and a sample rotation speed of 20 RPM.
Chemical etching (CE1)	Immersing in a solution made by mixing 50 mL H <sub>2</sub> O, 25 mL HNO <sub>3</sub> , and 5 mL HF for 120 s in an ultrasonic bath.
Chemical etching (CE2)	Immersing in a solution made by mixing 50 mL H <sub>2</sub> O, 25 mL H <sub>2</sub> SO <sub>4</sub> , and 25 mL HCl for 60 min in an ultrasonic bath.

and unique mechanical properties, that are either required for such biomedical applications or can be exploited to create unique functionalities. A negative Poisson's ratio and negative elasticity are some examples of such unique properties [26].

The improvement of the fatigue life of such open cellular lattice structures has been recently investigated as their poor dynamic behaviour is a limitation for the biomedical implant applications. Post-processing has been shown to be an effective approach for increasing the fatigue life. The effects of post-process heat treatments and surface modifications on the fatigue behaviour of such architected materials have, therefore, been extensively investigated [27–30]. Our previous work [31] in this regard was focused on microstructural design via heat treatments combined with surface modifications and their effects on the fatigue behaviour. Hot isostatic pressing (HIP) was found to be an effective heat treatment for improving the fatigue life of Ti6Al4V lattice structures due to the simultaneous application of isostatic pressure and elevated temperature [31–33]. The microstructure of materials and mechanical metamaterials substantially affects the mechanical properties of such porous structures [27,34]. Titanium, at room temperature, contains two main phases of  $\alpha$  and  $\beta$  [20,32]. The  $\alpha$  phase, which has a higher strength due to its hexagonal closed packed (HCP) crystal structure, undergoes an allotropic transformation through 882 °C ( $\beta$  transus) to a more ductile  $\beta$ -phase with a body centred cubic (BCC) crystallographic structure [21,35,36]. In the case of Ti6Al4V, Al acts as an  $\alpha$  phase stabilizer and V stabilizes the  $\beta$  phase [21]. Therefore, HIP was introduced as a suitable heat treatment to optimize the ratios of both  $\alpha$  and  $\beta$  phases, thereby providing a desirable combination of strength and ductility.

Understanding the relationship between microstructure and mechanical properties considering different scanning strategies and process parameters also plays an important role in the improvement and application of AM lattice Ti6Al4V. There is, however, currently a knowledge gap regarding the role of the scanning strategy (continuous (CLB) and pulsed laser-based (PLB)) on the fatigue life of 3D-printed lattice structures. Some comparative studies utilizing Ti6Al4V samples manufactured with continuous wave (CW) and pulsed wave (PW) laser modes have shown microstructural differences between the material resulting from those two scanning strategies. For example, the  $\alpha$  lath width is found to be smaller and more uniform for the PW types of scanning. Moreover, finer equiaxed grains have been found in the PW samples as compared to large columnar grains observed in CW [6,37,38]. However, the aforementioned works were conducted through DED additive manufacturing and investigated bulk solid structures.

Previous studies, which have been focused on other materials (e.g., AlSi10Mg, Ti, and stainless steel AISI 316 L) [39–41], have also shown the substantial effects of the scanning mode on the microstructure and properties of solid and porous specimens. The thermal history of the melt pool including the cooling rate and temperature variation has been found different for CW and PW modes, which leads to different texture

intensities and morphologies [40,42]. PW has been found to exhibit a smaller melt pool size and more controllability on heat input energy. However, its melt pool stability is lower because of the process intermittence. Therefore, PW was recommended for smaller and in particular lattice structures requiring less dimensional error, while CW can be more favourable for denser components with higher relative densities [43]. Overlapping between melt pools has been shown as another criterion for characterizing CW and PW. Process parameters such as hatch distance, scan speed, and layer thickness can all affect the overlapping quantity and morphology and determine the amount of process-induced porosity and roughness [42,44].

C. A. Biffi et al. have studied the effects of CW and PW on the microstructure and compression behaviour of solid AlSi10Mg. The compression behaviour of the materials processed using the CW strategy has been found to be less dependent on the building direction [40]. Ghouse et al. investigated stochastic porous Ti and stainless steel and the relation between laser parameters and scan strategies with respect to the strut thickness and mechanical properties. They confirmed that CW results in higher values of the compressive properties in comparison with PW [39].

There is, therefore, a clear knowledge gap regarding the microstructures resulting from both scanning strategies and their effects on the mechanical properties of as-processed lattice structures particularly their fatigue resistance. This study aims to provide a fundamental understanding of the effects of various post-processing on the microstructural anisotropy and fatigue behaviour of AM lattice structure made from Ti6Al4V using continuous and pulsed laser-based scanning strategies.

## 2. Materials and methods

### 2.1. Materials and manufacturing

Commercially available plasma atomized, spherical Ti6Al4V extra low interstitial (ELI) powder (AP&C Advanced Powder and Coatings Inc. Boisbriand, Canada) was used to fabricate lattice specimens with a cylindrical shape of  $\varnothing 15 \times L 20$  mm. The geometrical design included a diamond type repeating unit cells with a size of 1.5 mm (Fig. 1a). Diamond cell type was chosen based on findings from previous studies [15,45], where it showed isotropic behaviour and elastic modulus most comparable to the bone. Two types of L-PBF scanning strategies were applied in this study: (i) point or pulse laser-based, further denoted as group PLB and (ii) contour or continuous laser-based STL method, further denoted as CLB low or CLB high depending on their relative density. The L-PBF process parameters and powder characteristics used in this work for both scanning methods are presented in Tables 1 and 2.

Relative densities were determined by the dry weighting method, wherein the weight of the specimens is divided by the theoretical weight of the corresponding solid Ti6Al4V, assuming a theoretical density of 4.42 g/cm<sup>3</sup> [29]. The relative densities ranging between 14

**Table 4**  
The list of the relationships used for calculating the local stresses [26,47,48,66].

Formula (No.)	Designation	Parameters definition	Sample specific parameters
$\rho_{rel} = C_1 \left(\frac{L}{r}\right)^2 - C_2 \left(\frac{L}{r}\right)^3$ $\rho_{rel} = C_1 \left(\frac{L}{r}\right)^3 - C_2 \left(\frac{L}{r}\right)^4 \quad (2)$	Relative density	$C_1$ and $C_2$ : geometrical constants related to the unit cell type $L$ : strut length $r$ : strut radius	$C_1 = 4.8$ $C_2 = 3.2$ $L \sim 0.67$ mm
$F = \frac{F_{tot}}{nodes_2} \quad F = \frac{F_{tot}}{nodes_2} \quad (3)$	Strut force	$F_{tot}$ : total compression load on the sample with 2 nodes, where each node connects two struts	Nodes = 180
$S_1 = S_B - S_A = F \left( \frac{16L \cos \theta}{\pi d^3} - \frac{4 \sin \theta}{\pi d^2} \right) = F \cdot C_{sample} S_1 = S_B - S_A = F \left( \frac{16L \cos \theta}{\pi d^3} - \frac{4 \sin \theta}{\pi d^2} \right) \quad (4)$ $= F \cdot C_{sample} S_1 = S_B - S_A = F \left( \frac{16L \cos \theta}{\pi d^3} - \frac{4 \sin \theta}{\pi d^2} \right) = F \cdot C_{sample}$	Local stress	$S_1$ : maximum tensile stress component $S_A$ : axial compressive stress $S_B$ : Maximum bending stress $\theta$ : orientation of the strut force	$\theta = 37.5^\circ$

and 40 % were used in the current study, as shown in Fig. 1b. The relative densities of the samples were chosen based on the benchmark studies [15,27,29–31,34] about topological design and required porosity to achieve an elastic modulus close to that of the cortical bone.

Each of the aforementioned groups was divided into subgroups based on the applied post-treatment:

- i) As-processed specimens, used as the reference sample group (group AP)
- ii) Sandblasted samples (group AP–SB)
- iii) Specimens subjected to hot isostatic pressing (group HIP)
- iv) Specimens subjected to both HIP (applied first) and sandblasting (group HIP - SB)
- v) HIP specimens chemically etched with using solution 1 (group HIP - CE1)
- vi) Sandblasted HIP specimens chemically etched with solution 2 (group HIP - SB - CE2)

The details of the post-processing parameters used in the current study are presented in Table 3. It should be noted that after each post-treatment, the specimens were cleaned for 20 min in an isopropanol solution and 10 min in demineralized water in an ultrasonic bath.

## 2.2. Microstructural analysis

For cross-sectional microstructural analysis, two cutting directions were used, one parallel to the top surface and through the geometric centre of specimen and the other one at an angle of  $37.5^\circ$  to reveal the microstructure in the building direction. Sample preparation was performed by embedding the specimens in an epoxy resin followed by grinding (SiC 320, 800, 1200 and 2000) and polishing ( $3 \mu\text{m}$ ,  $1 \mu\text{m}$  with an oxide polishing solution (OPS) of  $0.04 \mu\text{m}$ ) for 10 min. In order to reveal the microstructure, the specimens were etched for 12 s in a solution made by mixing 50 mL distilled water, 25 mL  $\text{HNO}_3$ , and 5 mL HF. The microstructure was investigated by two optical microscopes (Keyence VHX5000 and Olympus BX60 M). The internal porosity determined using the digital method was estimated by dividing the porosity area over the total area of the strut cross-section. A scanning electron microscope (JOEL, JSM-6500 F, Japan) was utilized for morphological investigation of the lattice structure and strut thickness analysis. An automatic hardness Vickers machine (Durascan 70, Struers, USA) was applied to measure the microhardness on the cross-section of the polished specimens. A series of 10 measurements with a load of 0.3 kgf was carried out for each sample.

The electron backscatter diffraction (EBSD) technique was employed to investigate the grain size and crystallographic orientation of the different phases of AP and HIP specimens. The EBSD system was installed on an FEI- Quanta™ 450-FEG scanning electron microscope operated at 20 kV with a beam current of  $\sim 2.1$  nA corresponding to a spot size of  $5 \mu\text{m}$  for  $30 \mu\text{m}$  final lens aperture and 16 mm working distance. The EBSD specimens were prepared following the standard sequence of grinding and polishing steps with a final mechanical polishing step with colloidal silica solution (OPS – 35 nm particle size) diluted with 30 %  $\text{H}_2\text{O}_2$ . The EBSD patterns were acquired with a Hikari detector operated with the EDAX-TSL-OIM-Data Collection software (version 7.3) in a hexagonal scanning grid with a step size of 60 nm and 100 nm. The orientation data were post-processed using only the grain confidence index (CI) standardization procedure. The applied grain definition was: grain boundary misorientation higher than  $5^\circ$  and a minimum of 2 pixels per grain. The remaining points with the confidence index lower than 0.1 were excluded from the analysis. A numerical reconstruction of the parent  $\beta$  grains was made from the room temperature  $\alpha$ -phase EBSD data based on the existing Burgers orientation relationship between the body-centered  $\beta$  phase and the hexagonal  $\alpha$  phase with the help of the ARPGE 2.4 software [46].

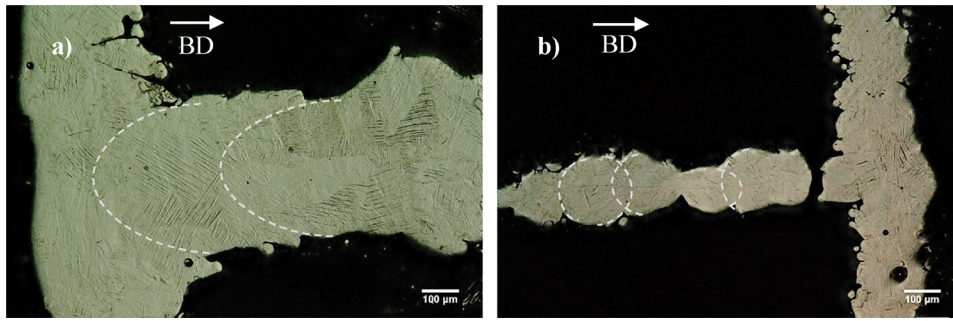


Fig. 2. Optical microscopy images of as-processed (a) CLB and (b) PLB specimens, indicating grain growth and melt pool boundaries.

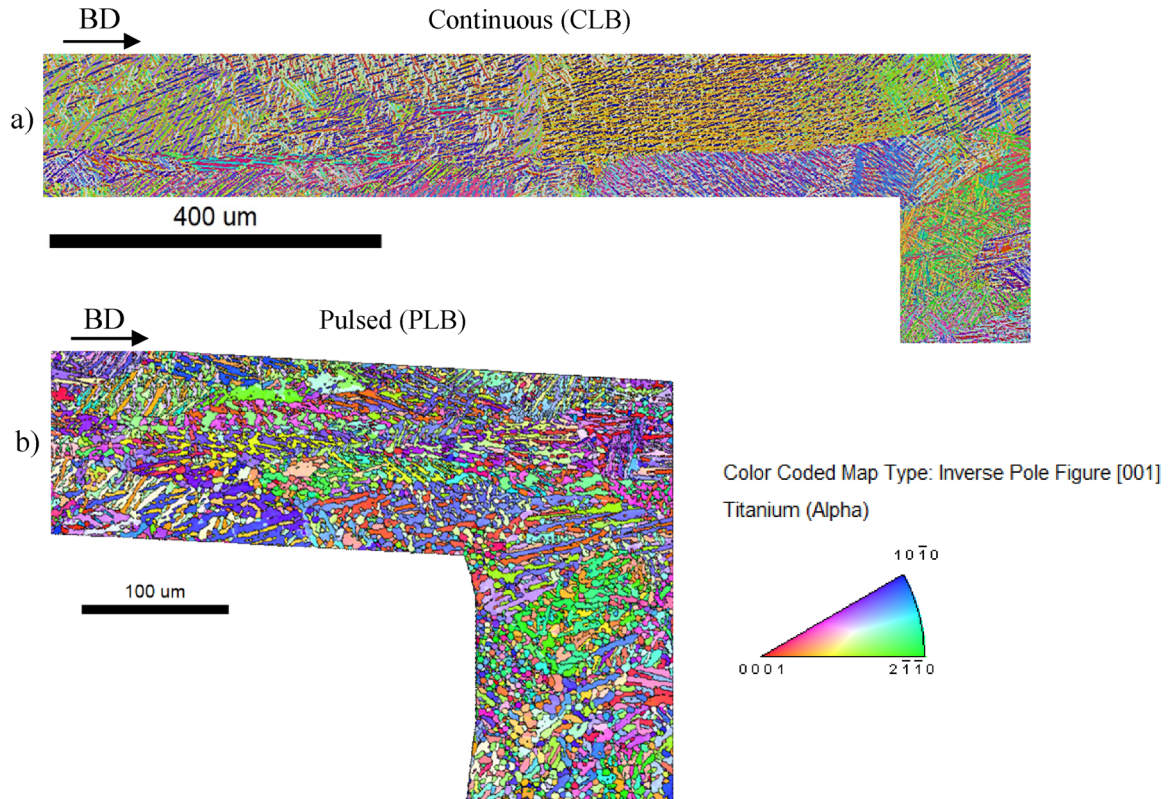


Fig. 3. EBSD inverse pole figure (IPF) maps of as-processed: a) CLB and b) PLB specimens, showing  $\alpha'$  grains orientation with respect to the building direction [001].

### 2.3. Static and dynamic mechanical testing

A mechanical testing machine (Zwick Z100, 80 kN load cell) with the strain rate of 1.8 mm/min and end criteria of 60 % deformation or 59 kN was applied to measure in compression the quasi-static mechanical properties of the specimens. Three specimens of each sample group were tested according to ISO 13314:2011 [47] for determining static mechanical properties (elastic gradient, plateau stress, compressive yield stress, compressive minimum principal stress). The mean static compression graphs were plotted using the mean stress values of a sample group at each strain increment of  $10^{-4}$  (mm/mm).

Compression-compression fatigue tests were conducted on all sample groups using a MTS 858 mechanical testing machine with a load cell of 100 kN, a load ratio ( $R$ ) of 0.1, and a frequency of 15 Hz. Three

fatigue tests were conducted for each sample group at eight different stress levels, ranging from 20 to 80 % of the yield strength. The end of test criteria was either 4 mm crosshead displacement or a 1 million cycles run-out.

### 2.4. Statistical and normalization methods

For the compression curves a 90 % confidence interval was calculated using Eq. (1) [48] to show the certainty of the mean compression graph considering the scatter in the samples:

$$CI = \bar{x} \pm 1.645 \frac{S}{\sqrt{n}} \quad (1)$$

Herein  $\bar{x}$  is the mean compression curve data point,  $S$  the standard

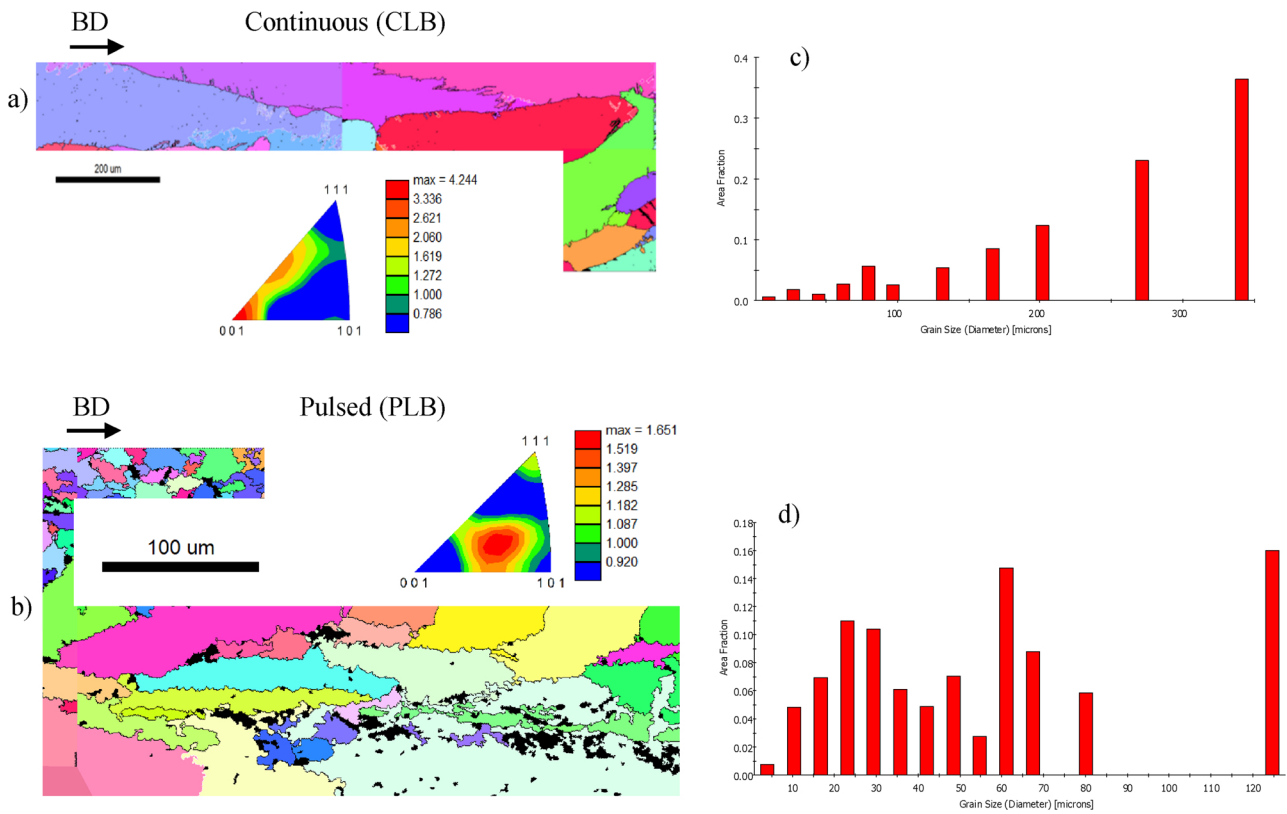


Fig. 4. The EBSD IPF map of vertical (along BD) and horizontal struts showing the reconstruction of the prior  $\beta$  phase for as-processed (a) CLB (b) PLB specimens, including the texture pole figure plotted in the BD orientation; The distribution of the grain size for the prior  $\beta$  grains in the (c) CLB and (d) PLB specimens.

Table 5

The grain size, volume fractions of  $\alpha$ , prior  $\beta$ , and retained  $\beta$  phases, based on the EBSD and SEM data.

Group type	$\alpha$ grain size, ( $\mu\text{m}$ )	Prior $\beta$ grain size, ( $\mu\text{m}$ )	$\alpha$ lath thickness, ( $\mu\text{m}$ )	Retained $\beta$ volume, (%)	Retained $\beta$ grain size, ( $\mu\text{m}$ )
CLB AP	$6 \pm 2.5$	$248 \pm 113$	$1.3 \pm 0.5$	< 1	–
PLB AP	$5 \pm 3.2$	$57 \pm 37$	$0.8 \pm 0.2$	< 1	–
-CLB HIP	$12 \pm 9.5$	$125 \pm 56$	$2.7 \pm 0.7$	2.5	$3.6 \pm 0.6$
PLB HIP	$8 \pm 4.7$	$31 \pm 14$	$4.6 \pm 0.8$	5	$1.7 \pm 0.9$

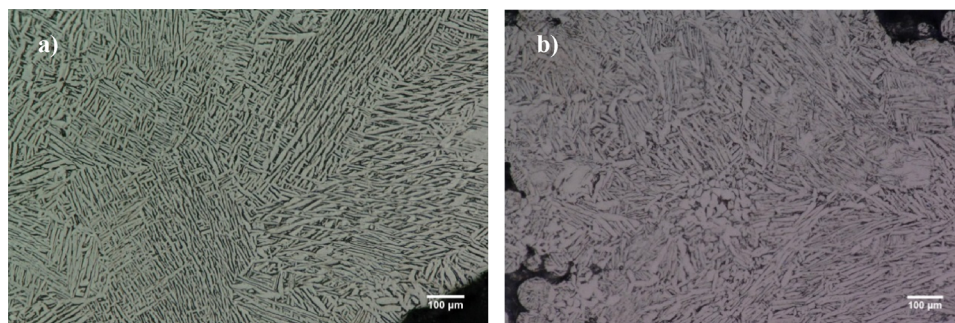


Fig. 5. The optical microscopy images of the HIPed (a) CLB and (b) PLB specimens.

deviation at point  $\bar{x}$  and  $n$  the number of samples.

A power law was fitted for each fatigue test group, using the non-linear regression capabilities in the Statistics and Machine Learning Toolbox of MATLAB (2017b, MathWorks, USA). Furthermore, using the

same toolbox for each S–N curve, a 90 % confidence interval was calculated and plotted with simultaneous bounds.

There were two types of mechanical test data normalization used in the current work:

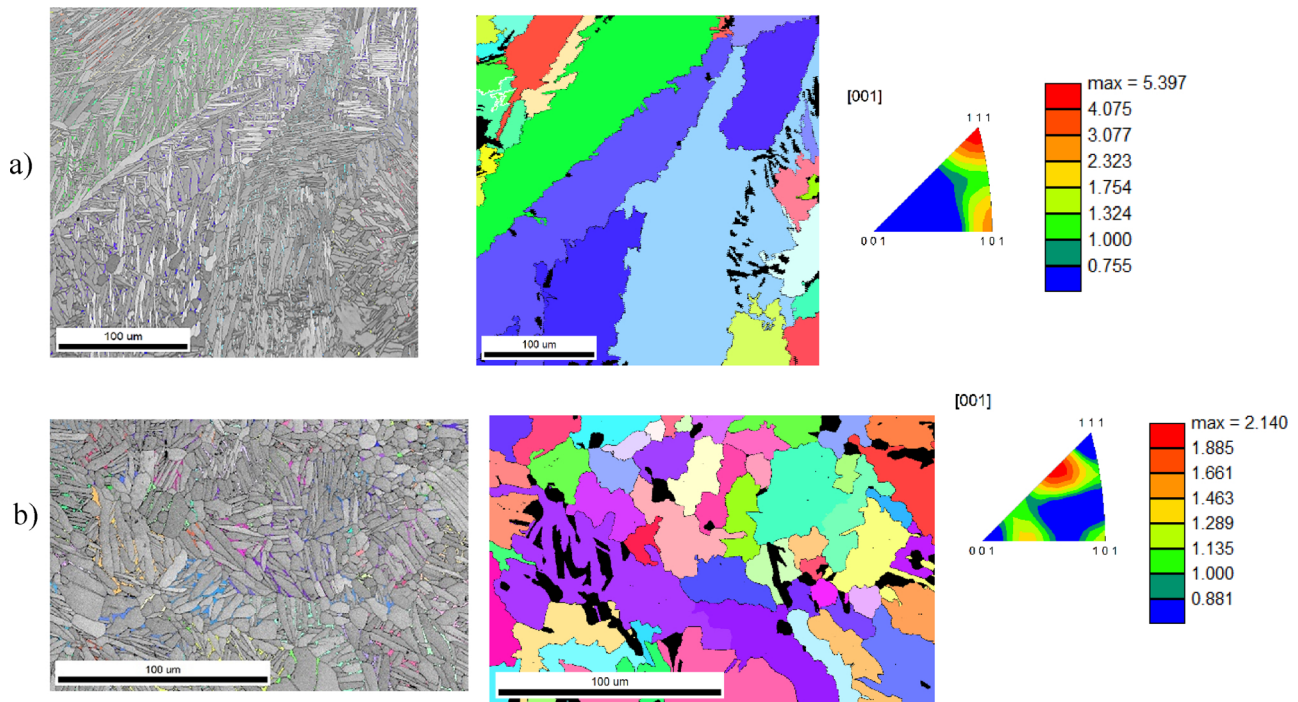


**Fig. 6.** The combined EBSD image quality and inverse pole figure maps of the HIPed specimens produced using (a) CLB and (b) PLB modes visualizing the retained  $\beta$  (in colour) and prior  $\beta$  grains along the [001] direction.

**Table 6**

The microhardness and internal porosity of CLB and PLB and the effects of HIP.

Sample	Internal porosity (%)	Hardness (HV <sub>0.3</sub> )
CLB AP	0.41 ± 0.24	401 ± 21
CLB HIP	0.04 ± 0.07	361 ± 13
PLB AP	0.98 ± 0.87	421 ± 24
PLB HIP	0.18 ± 0.19	357 ± 19

- Fatigue data were normalized by dividing the applied stress by the 0.2 % offset yield stress obtained from quasi-static mechanical tests (further denoted as normalization with respect to the yield stress).
- The analytical normalization method proposed by Hooreweder et al. [28] was applied for normalizing both static (stress-strain curves) and dynamic (S-N curves) compression mechanical tests based on the local stress approach. The local stress is the stress experienced by a single strut, which gives a better approximation of the true stress. The formula used for the calculation of the local stress and the relevant parameters that are dependent on the sample characteristics are listed in Table 4. We refer to this technique as normalization with respect to the local stress.

In order to have a better understanding of the fatigue behaviour of the different scanning modes and post-process conditions, the fatigue lives lower than  $10^5$  cycles were studied as low cycle fatigue (LCF) and between  $10^5$  and  $10^6$  as high cycle fatigue (HCF).

### 3. Results and discussion

#### 3.1. Microstructural characterization of CLB vs. PLB lattice structures

The optical and EBSD images of as-processed CLB in the build

direction (BD) plane are shown respectively in Fig. 2a and 3a. Hierarchical hexagonal  $\alpha$  laths were visible within elongated columnar prior  $\beta$  grains. In addition, preferential orientation was observed for the  $\alpha$  laths generated from grain boundaries (Fig. 3a). The observed preferential texture of AM CLB material is associated with the solidification processes, which includes thermal gradients and other physical phenomena, such as vaporization and heat transfer. Solidification modes can be planar, cellular, columnar dendritic or equiaxed dendritic, depending on the undercooling and thermal gradient conditions [51]. Using the CLB mode, new crystalline layers were formed with a well-defined orientation, parallel to the maximum thermal gradient (i.e., building direction (BD)), which is called epitaxial grain growth. As seen in Fig. 2a, boundaries of prior  $\beta$  grains were found to be elongated along the building direction, which is in line with the findings of previous studies [40,51–53].

In the PLB specimens, a basket-wave morphology with interleaving  $\alpha$  laths was observed through equiaxed grains (Figs. 2b, 3b). A higher width, depth, and shape of the melt pool in PLB lead to different fluid flow conditions, which is related to a higher laser power and exposure time [42,54] in comparison with the CLB mode. In the PLB process, the surface tension (Marangoni effect) and buoyancy force enhance heat transfer and cause two vortices within the ellipse-shaped molten pool. Whereas the thermal cycle is different in the case of CLB and just one vortex stirs the molten pool and forms a comet-shaped melt pool [51,54]. As a result, the PLB molten pool is affected by the higher cooling rate rather than the CLB, which leads to finer equiaxed dendritic  $\alpha$  grains with no preferential orientation (Fig. 3b) as well as finer and more equiaxed prior  $\beta$  grains (Fig. 4b).

Numerically reconstructed prior  $\beta$  grains and its size distribution for both CLB and PLB (Fig. 4a and b) confirm the relationship between the direction of grain growth and scanning strategy. For CLB mode parent  $\beta$  grains are elongated along the building direction with a strong < 001

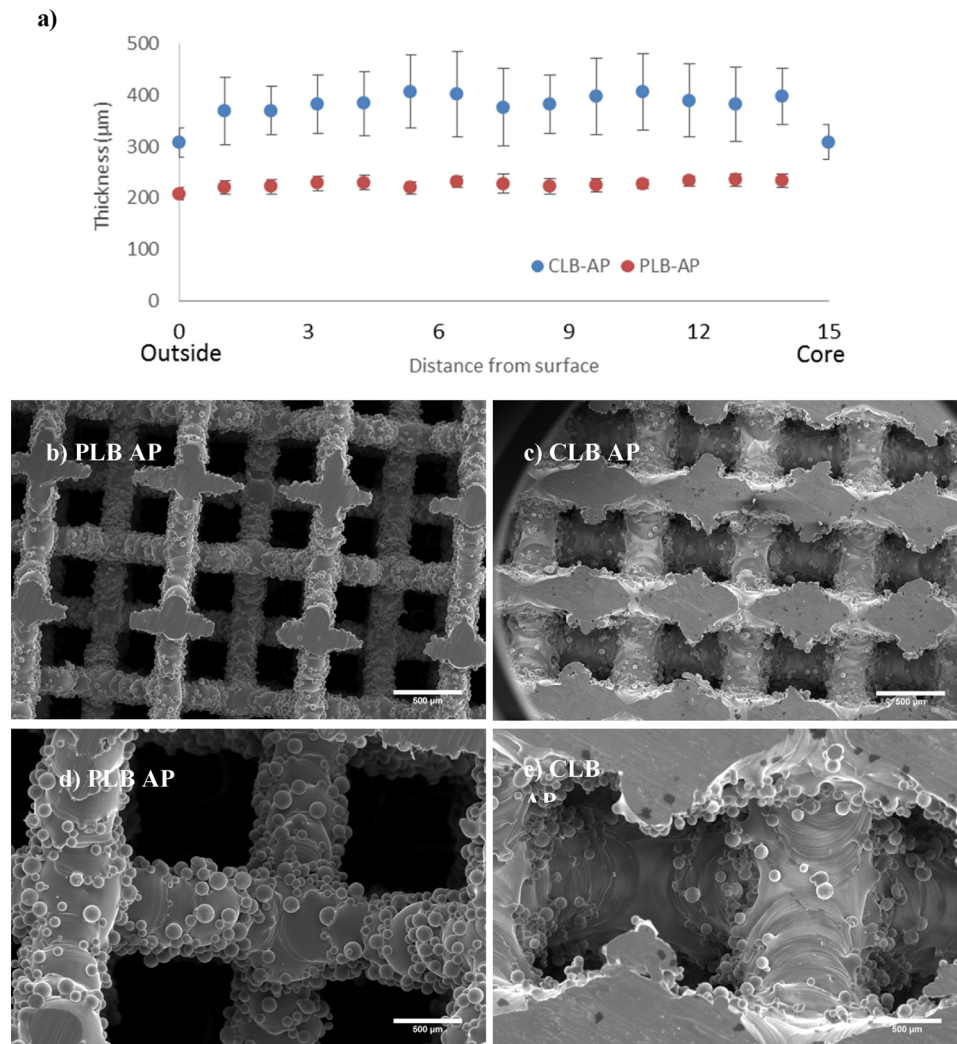


**Fig. 7.** The morphological characterization of as-processed samples showing a) strut thickness from the surface to the core of CLB vs. PLB; b), c), d) and e) illustration of partially molten particles at the sample core.

> texture, resulting in highly anisotropic columnar microstructure. Most of these columns are separated by high angle grain boundaries ( $> 15^\circ$ ). The  $\beta$  phase is dependent on the high cooling rate either for bulk or lattice structure AM Ti6Al4V, and can be transformed completely into a mixture of acicular martensitic  $\alpha'$  or  $\alpha/\alpha'$  microstructure [31,63,71]. It should be noted that  $\alpha$  and  $\alpha'$  grains have a similar composition. However,  $\alpha$  has more dislocations due to the solidification-induced thermal stresses. In the case of the lattice structure, the cooling rate in the struts is even higher due to the smaller melted area and lower latent heat [53]. As compared to CLB, the PLB mode has no preferred texture and generates equiaxed and finer  $\alpha'$  laths and prior  $\beta$  (see Table 5) with a more consistent thickness and, thus, a more uniform microstructure, which is a result of a higher cooling rate. Furthermore, previous studies of CLB have found that the  $\alpha'$  lath size varies and with the degree of variation increasing when moving from the surface to the core of the strut [6,53].

During the HIP, in which the temperature is elevated to 920 °C (just below the  $\beta$  transus temperature of 996 °C [55]), acicular  $\alpha'$  martensitic structure transforms to fine-scale  $\beta$  and an elongated  $\alpha$  phase. At the

beginning of the HIP process, the  $\alpha$  phase precipitates along the  $\alpha'$  boundaries. By growing  $\alpha$  plates, vanadium (as  $\beta$  stabilizer) withdraws to an adjacent region and  $\beta$  nucleates owing to V enrichment. For both CLB and PLB, the final microstructure after HIP consisted of a mixture of elongated  $\alpha$  platelets embedded in  $\alpha/\beta$  grain boundaries (Figs. 5 and 6) [56,57].

Continuing heat treatment from lower temperatures led to the segregation of Al into the  $\alpha$  phase and the diffusion of V into  $\beta$ , which can cause the coarsening of the lamellae structure [58]. In this work 5 and 2.5 % of retained  $\beta$  for CLB and PLB, respectively, were found (Table 5). The morphology and size of  $\alpha$  plates and  $\beta$  precipitates have an important effect on the mechanical properties of the lattice structures. Higher crack propagation resistance is likely induced from columnar and lamellar  $\alpha/\beta$  in CLB HIP (Fig. 5a) in particular with a lower  $\alpha$  lath thickness in comparison with PLB (Table 5). In contrast, equiaxed or bimodal microstructure in PLB HIP (Fig. 5b) has been reported to have a lower threshold and less sensitivity to crack initiation [59,60]. Martensitic  $\alpha'$  has been shown to result in a higher yield stress and a higher ultimate tensile strength, but lower ductility. Therefore, by

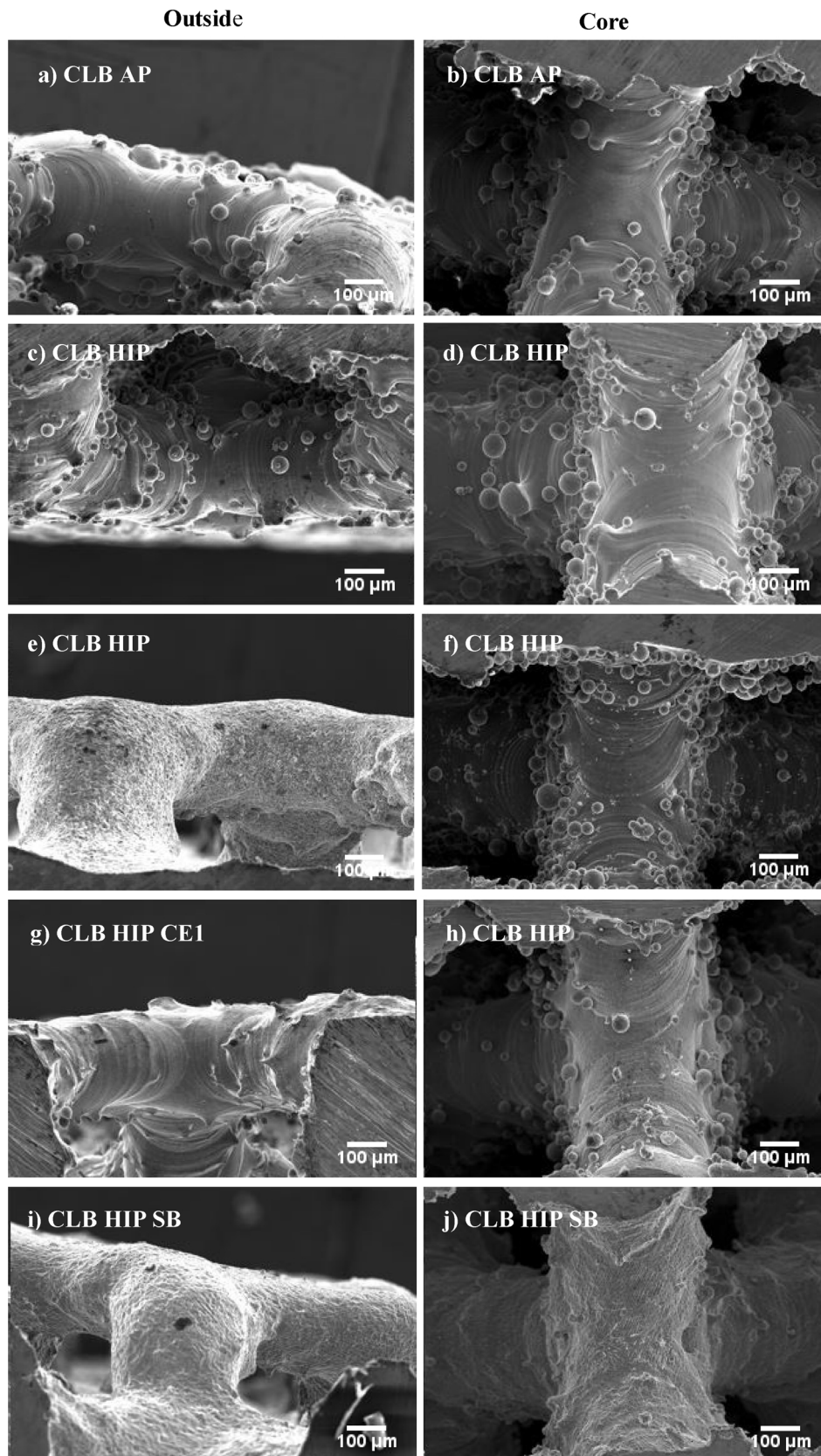
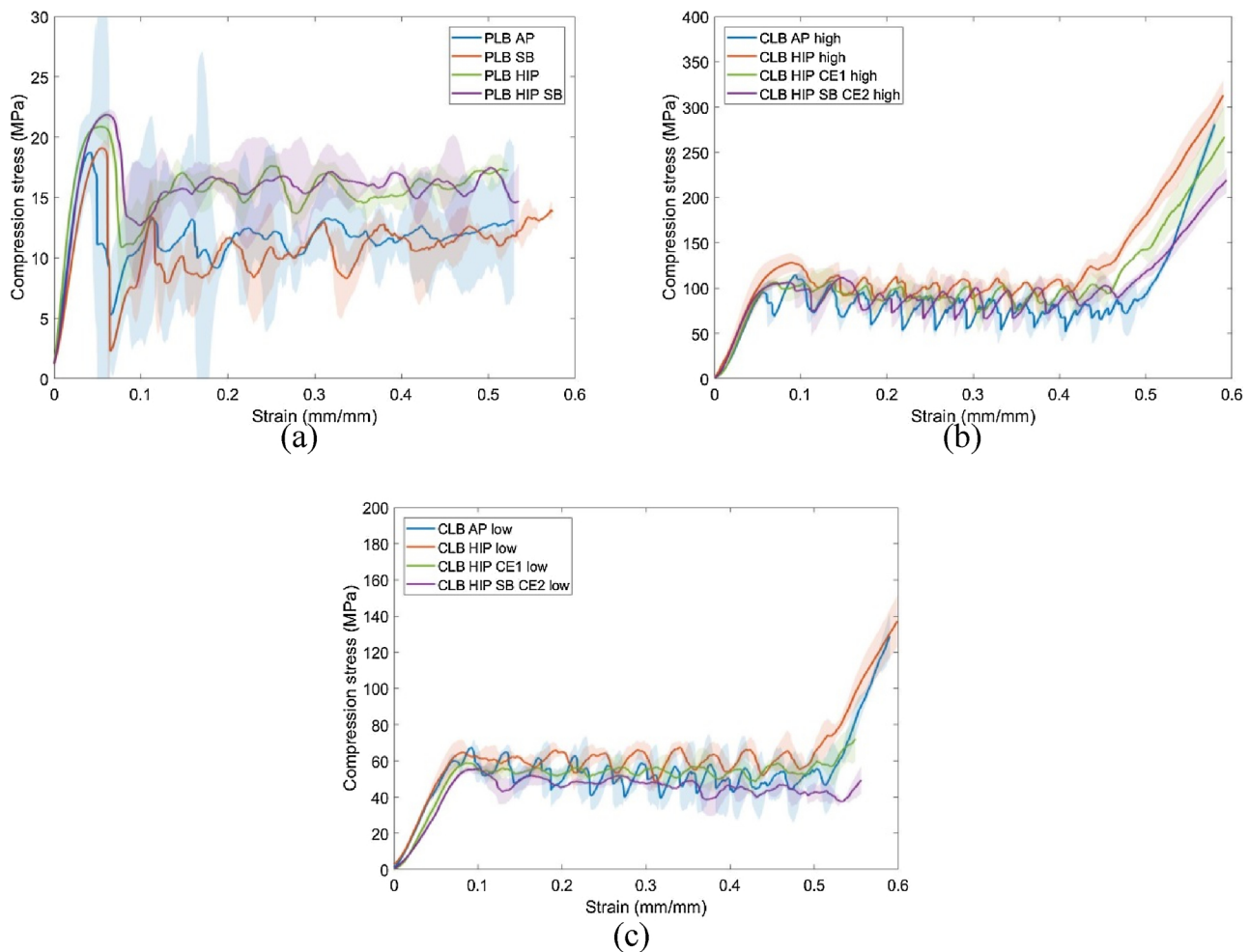


Fig. 8. The surface modified lattice structures manufactured using the CLB process subjected to different post-processing treatments.



**Fig. 9.** The mean compressive stress-strain curves measured for lattice structures with and without the various types of post-treatments. All curves are accompanied with zones depicting the 90 % confidence intervals: (a) PLB, (b) CLB-High, and (c) CLB-Low.

transforming to a lamellar  $\alpha/\beta$  microstructure with retained  $\beta$  enhancement (5 and 2.5 % for CLB and PLB, Table 5), the ductility and, subsequently, dynamic mechanical properties of the resulting materials could be improved (Fig. 10), which will be discussed further in the follow-up sections. It should also be noted that besides grain coarsening (Table 5, Fig. 5), HIP also resulted in changes to  $\langle 111 \rangle$  preferential texture of prior  $\beta$  for the CLB specimens, while PLB produced fully equiaxed microstructures with no preferred orientation (Fig. 6).

The microhardness of as-processed PLB samples was slightly higher than CLB, which is caused by the smaller  $\alpha$  grain and lath size (Tables 5 and 6). The observed presence of internal porosity is likely to have an important effect on the mechanical properties of the lattice structures and, thus, requires further investigation. As-processed PLB incorporated a higher amount of porosity (Table 6), which could be related to such previously reported process parameters as hatch distance and layer thickness [42,53,61]. PLB samples were found to be more affected by HIP, resulting in substantial reduction of both hardness and internal porosity due to the simultaneous application of heat and pressure [60]. Lower microhardness for all HIP samples can be explained by the transformation of the needle shaped  $\alpha$  to lamellar  $\alpha/\beta$  and the appearance of a more ductile  $\beta$  phase [62,63].

### 3.2. Morphological surface characterization

A more uniform strut thickness was observed in PLB, while for CLB the thickness increased from the surface to the core (Fig. 7a). The strut thickness (also known as diameter) has been reported to be related to the melt pool size, which can be affected by different process parameters [53]. In CLB, the laser power, scan speed, and hatch distance control the melt pool size, which is in contrast with the PLB where laser power and exposure time play the most important roles [64]. Thus, a better control of heat input in PLB can lead to a more controlled solidification kinetics, giving further possibilities for microstructure optimization [72]. Increasing the hatch distance and layer thickness can lead to the instability of the melt pool due to the Marangoni force and recoil pressure. Therefore, the porosity and roughness could increase owing to melt pool instability [44,65]. For CLB, the remelting strategy was recommended in some studies to reduce process induced porosity and increase crystallographic texture [69,70].

Variations in the building angle may be the other parameter affecting the roughness and diameter of the struts for both CLB and PLB [64,66]. In the current study, the strut diameter was found to be more uniform in PLB (Fig. 7a) owing to more controllability of the process

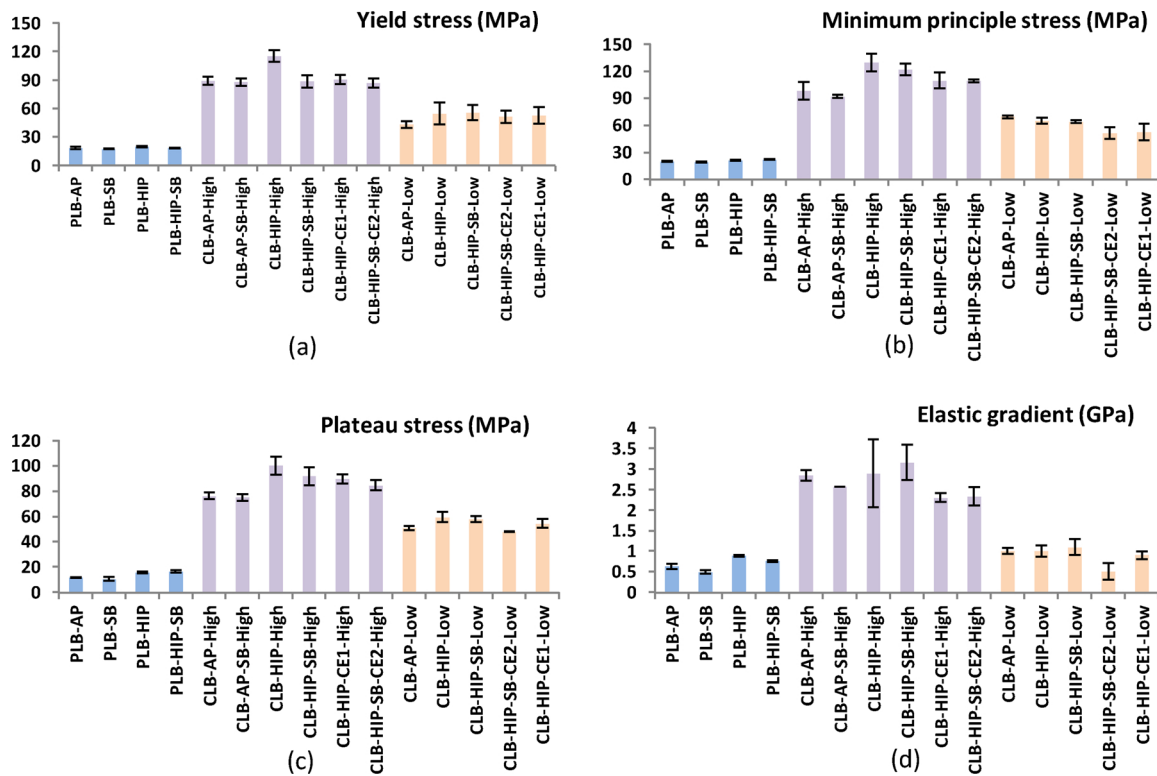


Fig. 10. The compressive quasi-static mechanical properties of the lattice structures made using different processes and subjected to the various types of post-processes: (a) yield stress, (b) minimum principle stress, (c) elastic gradient, and (d) plateau stress.

parameters. Therefore, CLB can be in general recommended for larger and denser parts, whereas PLB is suggested for smaller and more precise components, such as lattice structures [39–43].

During the L-PBF process, such defects as porosity, unmolten, or partially molten particles and balling can emerge. Partially molten particles can act as stress concentration points that adversely affect the fatigue behaviour of the lattice structures. Fig. 7 compares the surface morphology of the struts between PLB and CLB and illustrates the increased presence of partially molten particles in the PLB case (see Fig. 7b and d). The occurrence of partially molten particles was found to be more frequent in the PLB mode, which is likely due to melt pool instability and an intermittent melting process [43].

In the CLB mode, since the process power is constant, the melt pool is more stable and the amount and intensity of partially molten particles are lower. Figs. 7e and 8 show the impact of the applied surface modifications on the outside and core of the CLB specimens. An optimized abrasive particle size of 50  $\mu\text{m}$ , a blasting duration of 90 s, and a pressure of 4.5 bar were applied in the current study to improve penetration to the core of the sample in comparison with our previous study [29]. Furthermore, a less aggressive etchant, namely  $\text{HCl} + \text{H}_2\text{SO}_4$  (CE2), was used for 60 min (Fig. 8i and j), since in our previous work HF showed limited penetration and air trapping [29]. HIP affected the surface of the struts through a densification process that decreased the process-induced porosities. However, it had no visible effects on partially molten particles (Fig. 8c and d). A combination of HIP and SB showed more influence on the top rather than the core of the specimens (Fig. 8e and f). A combination of the three post-processing methods of HIP, SB, and CE2 was found to best remove the partially molten

particles while resulting in the least detrimental effects in terms of material removal (as in the case of HIP-CE1) (Fig. 8i, j), thereby delivering a homogenous through-the-sample core strut thickness.

### 3.3. Quasi-static mechanical properties

#### 3.3.1. Global compressive behaviour

Comparison of the linear parts of the global stress-strain curves shows an improvement of the yield stress, elastic gradient, and minimum principle stress after HIP for all specimens (Figs. 9 and 10), which is attributed to the change from a brittle acicular  $\alpha$  phase to lamellar (PLB) or columnar (CLB)  $\alpha/\beta$  and reduction in porosity. Surface modification by SB and CE generally resulted in a slight decrease of the mechanical properties (Figs. 9 and 10), which is caused by the weight reduction. Comparing the laser modes, one can notice that the CLB specimens exhibit the classic three-stage stress-strain behaviour (Fig. 9b, c), while the specimens manufactured with PLB mode did not reach the densification stage within the test strain range (Fig. 9a). The CLB specimens (both high or low density) showed considerable fluctuation in their plateau region, specifically for the AP and AP SB conditions (Fig. 9b and c), as compared to the PLB specimens. This fluctuation is typical for brittle component [68,49,50] while the smooth plateau region in PLB could be attributed to the finer microstructure of the PLB specimens, which consists of more equiaxed, bimodal grains and finer  $\alpha / \alpha$  laths.

#### 3.3.2. Normalized compression behaviour

There is a significant difference in the compressive quasi-static

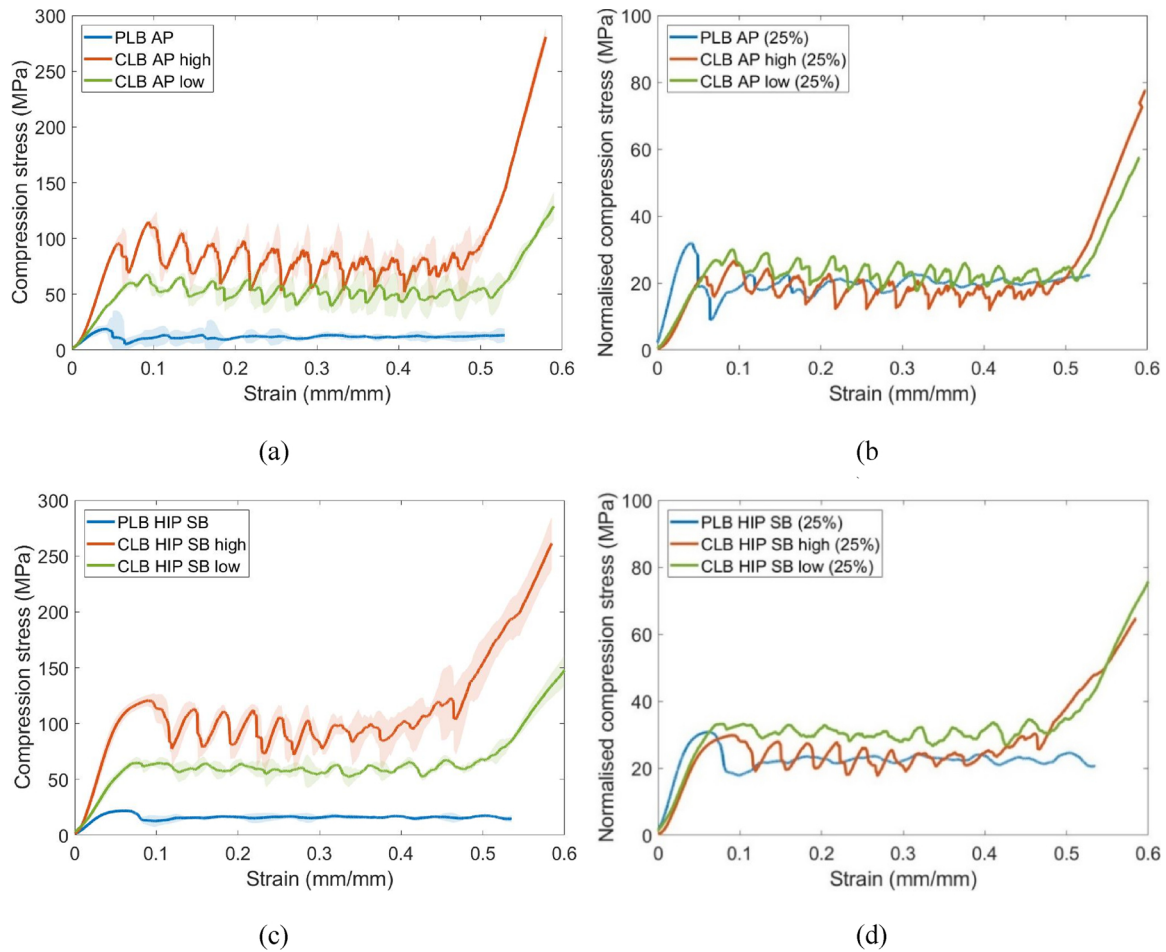


Fig. 11. Global (a, c) vs normalized (b, d) compressive stress-strain curves measured for lattice Ti6Al4V structures with 90 % confidence interval for (a, b) PLB, CLB High, and CLB Low AP and (c, d) PLB, CLB High and Low HIP-SB.

mechanical properties between the three considered groups, namely PLB, CLB-low, and CLB-high, which is due to the differences present in their relative density and strut thickness (Figs. 10 and 11). In order to have a more accurate comparison between the different scanning methods, a normalized quasi-static compression behaviour depending on the local stress was further investigated (Fig. 11). The normalized curves revealed that the yield stress and elastic gradient are higher for the PLB samples (Fig. 11b), which could be explained by the higher cooling rate experienced by those specimens, which leads to a finer microstructure and more retained  $\beta$  fraction in the re-melted region [53]. Therefore, based on the Hall-Petch relation, the elastic behaviour of the AP PLB specimens is superior to that of the CLB specimens (except for the densification zone). This trend disappears after HIP and SB, which results in an overall similar elastic behaviour for both PLB and CLB specimens (Fig. 11d).

### 3.3.3. Fatigue behaviour

The global S-N curves comparing the different scanning methods show the inferior fatigue behaviour of the PLB group (Fig. 12a), which is likely attributed to its lower relative density (Fig. 1) and strut thickness (Fig. 7a). Regarding the effects of post-processing, similar trends can be observed irrespective of the applied scanning method: (i)

the AP samples showed lowest and HIP specimens exhibited the highest fatigue resistance; and (ii) no significant effects were visible after SB and CE treatments. For instance, a combination of SB and CE2 not only did not improve the fatigue resistance, but actually reduced it for both CLB low and high (Fig. 12a, b), which is related to the critical weight and the reduction in the strut thickness.

An improvement is, however, visible for HCF as compared to LCF after the combination of CE1, CE2 and SB (Fig. 12c). In order to more clearly demonstrate the gap between the global fatigue curves of the different scanning techniques, a representative combination, namely the HIP SB group, is further highlighted in Fig. 12d.

The normalization of the S-N curves is required to provide a better comparison between the different scanning modes and post-processing conditions (Fig. 13). The S-N curves normalized with respect to the 0.2 % offset yield stress (obtained from the quasi-static stress-strain curves) pointed towards the same conclusion that the normalized fatigue properties of the PLB specimens are inferior to those of the CLB specimens (Fig. 13a). However, the normalization step reduced the difference between the different scanning modes (Fig. 13a) as compared with the global S-N curves (Fig. 12a). For both LCF and HCF, the same post-processing trend was observed, namely HIP SB and HIP CE1 improved the fatigue life of both PLB and CLB specimens. The S-N curves (both

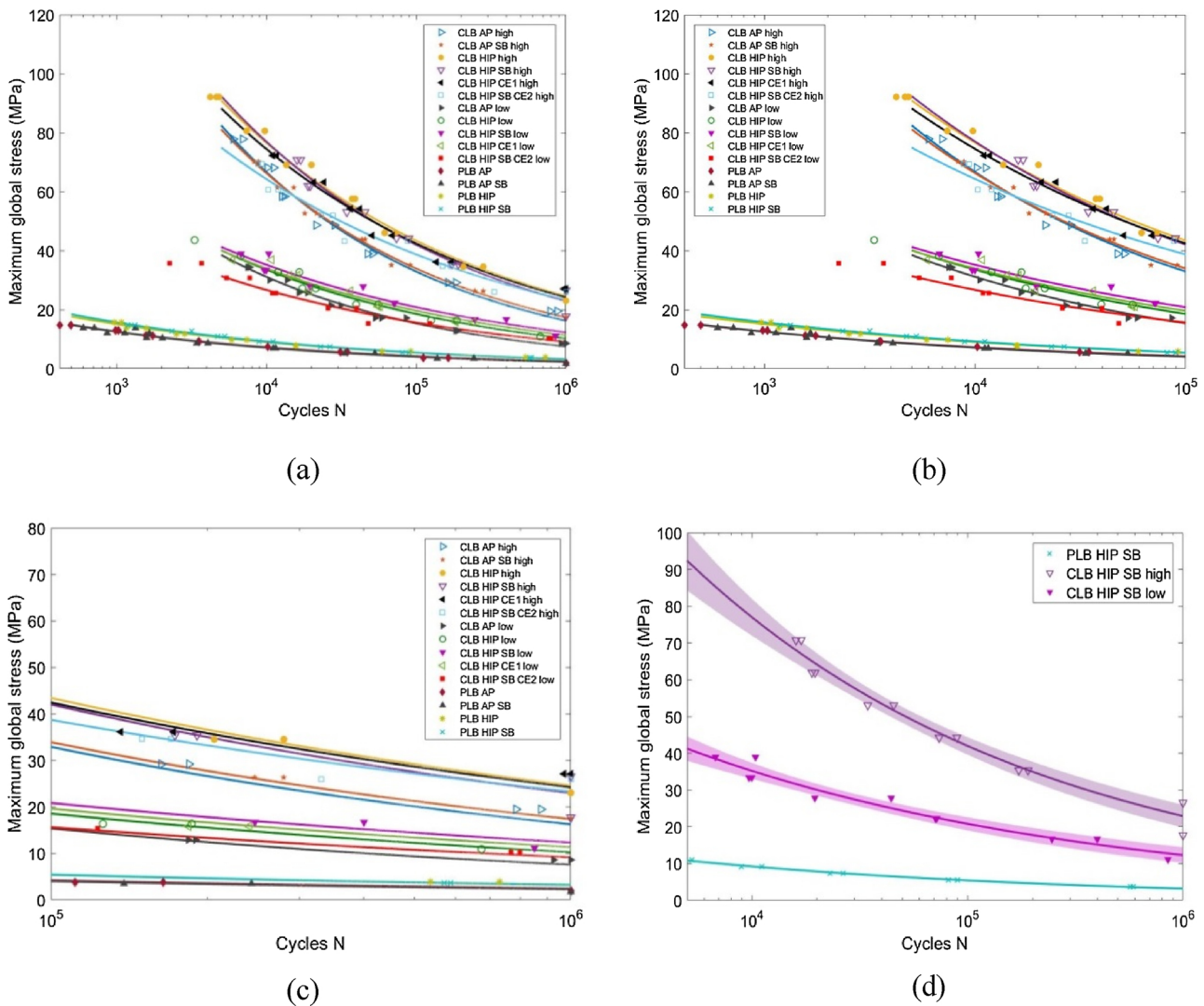


Fig. 12. The global S-N curves of lattice Ti6Al4V structures for the different scanning methods and post-processes and displayed as (a) full S-N curves (b) LCF, (c) HCF) and (d) A comparison between PLB, CLB-high and CLB-low subjected to HIP and SB with 90 % confidence interval.

global and normalized with respect to the yield stress) still exhibited uncertainties arising from the differences caused by the different values of the relative density and strut thicknesses.

In order to represent the true bulk properties and, thus, the stress experienced by a single strut, a different type of normalization method [28] was used. This method, which we refer to as the local stress normalization technique, uses the calculated strut thickness, which is subsequently applied in maximum local tensile stress calculation. Therefore, this normalization technique allows to account for changes in the relative density, scanning methods, and surface treatments. It should be, however, noted that this technique uses an approximation of the true stress, since other effective parameters, such as the stress concentration points, surface morphology, residual stress, and process-induced porosity are not included.

### 3.3.4. Fatigue normalized with local stress: LCF vs. HCF

Fig. 14 a and b show the S-N curves that are normalized with respect

to the local stress. Even with this normalization method, the PLB samples show lower cycles to failure as compared to the specimen using the CLB mode. This could be explained by the higher percentage of process-related defects introduced into the struts (Table 6) and partially molten particles (Fig. 7b and d), both of which play important roles in fatigue crack initiation. The most significant difference between this normalization technique and normalization with respect to the yield stress was observed for the CLB group (Fig. 14) with a combined treatment of HIP SB CE2 showing improved fatigue behaviour and reduced scatter for both CLB low and high. Therefore, process-induced imperfections, which serve as crack initiation sites, can be successfully treated by this post-processing combination, where: (i) HIP decreases the internal porosity and simultaneously changes the brittle acicular  $\alpha$  phase to lamellar  $\alpha/\beta$  and increases the amount of more ductile  $\beta$  phase and (ii) SB and CE2 remove partially molten particles that act as stress concentration points.

It is worth noting that, in both LCF and HCF regimens, post

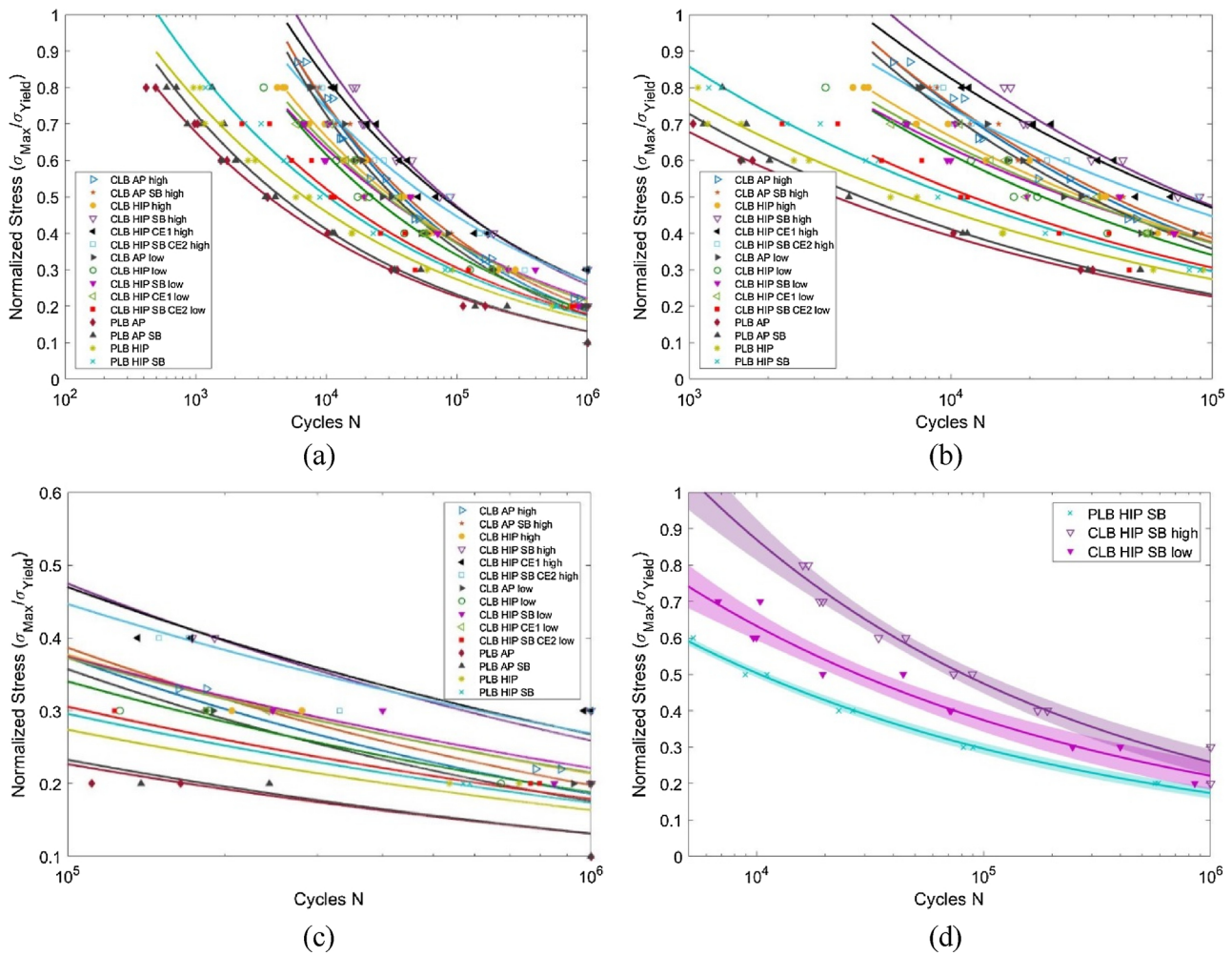


Fig. 13. The S-N curves normalized with respect to the 0.2 % offset yield stress showing (a) a comparison of different scanning methods and post-processes (b) LCF (c) HCF and (d) a comparison between PLB, CLB-high and CLB-low subjected to HIP and SB with 90 % confidence interval.

processing combination (HIP SB CE2) performed here is more effective for improving the fatigue lives of the lattice structures as compared to HIP SB and HIP CE1 which has been reported in the literature [28,31]. This is likely due to the more optimized SB and CE treatment protocols used herein, which results in better penetration of the SB particles and the etchant liquid (Fig. 8).

The PLB specimens were found to also have an inferior fatigue behaviour in the HCF range. Only with the application of HIP SB, the S-N curves of the PLB specimens reached those of as-processed CLB (low and high). In the case of the CLB specimens, HCF was also significantly improved after HIP SB CE2 post-treatment. The effects of this combination could be explained by the influence of each post-processing (addressed in the previous section), which hinders crack propagation, known to be of critical importance for HCF failure.

A summative schematic comparison between PLB and CLB laser tracks, addressing the affects the grain growth, surface defects and fatigue crack initiation sites, is illustrated in Fig. 15. The CLB mode resulted in comet-like melt pools, while PLB created ellipse-like melt pools with re-molten overlap areas [52]. The laser track and melt pool morphology were found in [51,53,54], to be related to the heat gradient

in the building direction. Fatigue cracks were found in this work to have initiated at the struts junctions, known to be the stress concentration points [67], in the case of the lattice structures made using the CLB mode (Fig. 15 c). The PLB mode, however, showed fatigue initiation between the subsequent beads (Fig. 15 d), which is related to a finer and more homogeneous  $\alpha$ -lamellar microstructure with higher hardness after re-melting contrary to the hierarchical  $\alpha$  laths in the adjacent single molten region [53]. Therefore, this difference in fatigue failure initiation is likely caused by microstructural variations along the PLB struts as well as the concentration of residual stresses in the re-molten region.

#### 4. Conclusions

In this study the difference between the continuous and pulsed L-PBF scanning strategies and their effects on the microstructure and mechanical behaviour of AM Ti6Al4V lattice structures was investigated. Additionally, the influence of various post-processing heat treatments and surface modifications on the fatigue life of the lattice structures was studied. The following conclusions can be drawn from

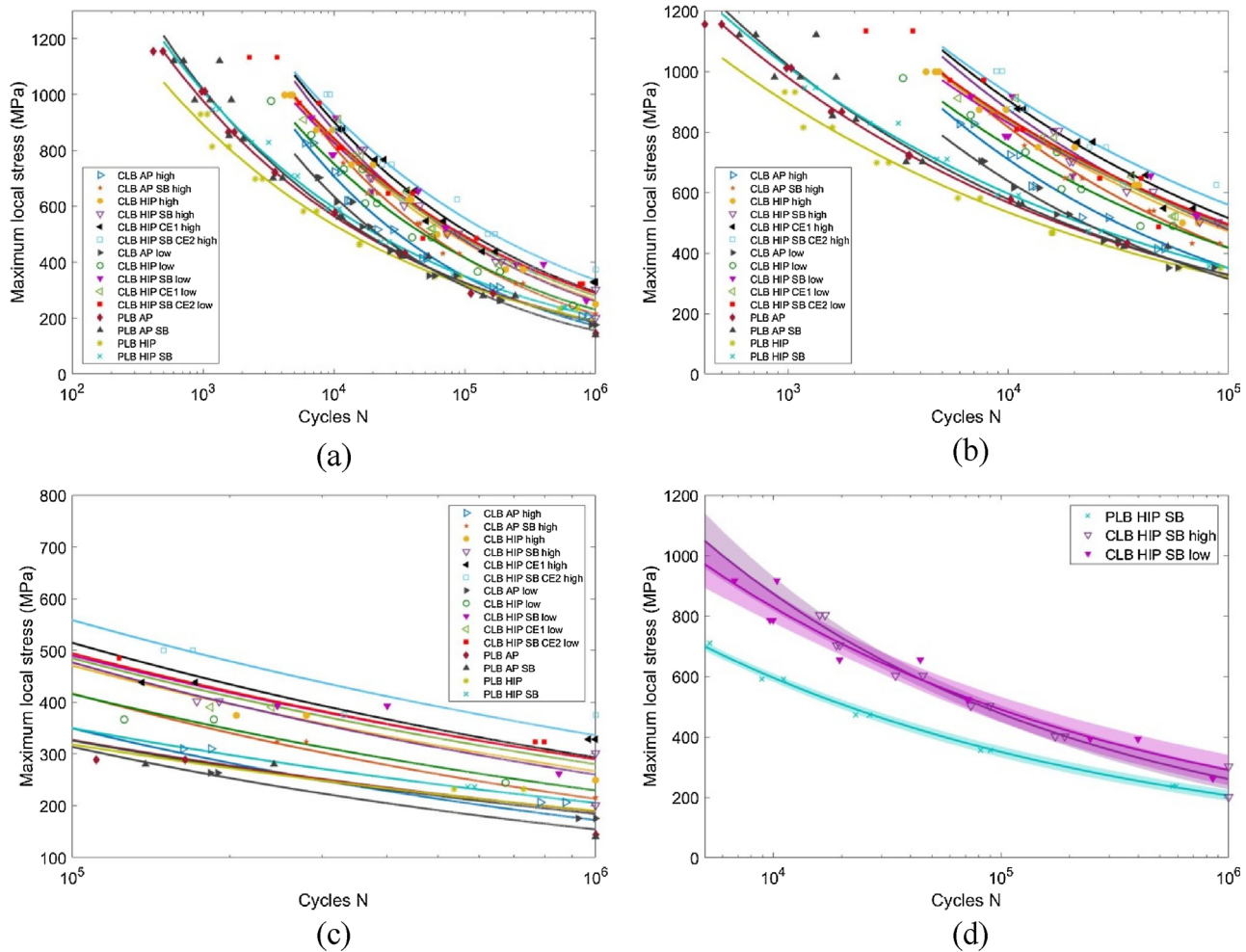


Fig. 14. The S-N curves normalized to local stress displayed as (a) full curves (b) LCF (c) HCF and (d) a comparison between PLB, CLB-high and CLB-low subjected to HIP and SB with 90 % confidence interval.

our results:

- The size and orientation of acicular  $\alpha$  and prior  $\beta$  grains as well as the fraction of retained  $\beta$  were found as the main microstructural differences between continuous and pulsed laser modes, leading to differences in the hardness, strength, and fatigue life.
- The compressive mechanical properties, in particular normalized yield stress, were found to be higher for pulsed laser due to a more homogenous and finer microstructure and isotropic properties. It should, however, be noted that pulsed samples did not exhibit the characteristic densification zone, due to full or partial disintegration into powder.
- The strut thickness was found to be more uniform for pulsed laser. This scanning mode can, therefore, be suggested for smaller components where dimensional accuracy is required (e.g., lattice structures) in comparison with continuous laser, which might be more suitable for larger and denser parts. It should, however, be pointed that due to a high amount of porosity and number of partially molten particles, the process parameters of the pulsed mode process should be further optimized.
- The process employing a continuous laser scanning mode resulted in a higher level of fatigue life, which is related to fewer process-induced imperfections and the higher resistance of the underlying microstructure against crack propagation.
- Local stress normalization was found to be the most effective method to study the mechanical response of lattice structures, as it enables taking into account the differences in the relative density

and strut thickness. However, the proposed numerical normalization method can be further improved by considering the relevant geometric parameters and different imperfections.

- Inter-beads failure was detected among the struts manufactured using pulsed laser scanning mode, contrary to the continuous mode where mostly nodes intersections were reported as stress concentration points. Further investigation into stress concentration and the failure mechanisms of continuous and pulsed strategies is required.
- Regarding the applied herein post-processing, a combination of hot isostatic pressing, sand blasting, and chemical etching was found as the most effective way for improving the fatigue behaviour of lattice structures made from Ti6Al4V.

#### CRediT authorship contribution statement

**K. Karami:** Writing - original draft. **A. Blok:** Methodology, Formal analysis, Data curation, Writing - review & editing, Investigation. **L. Weber:** Investigation. **S.M. Ahmadi:** Resources. **R. Petrov:** Visualization. **Ksenija Nikolic:** Visualization. **E.V. Borisov:** Investigation. **S. Leeflang:** Resources, Writing - review & editing. **C. Ayas:** Writing - review & editing. **A.A. Zadpoor:** Resources, Writing - review & editing. **M. Mehdipour:** Investigation. **E. Reinton:** Investigation, Methodology. **V.A. Popovich:** Conceptualization, Supervision, Project administration, Writing - original draft, Writing - review & editing.

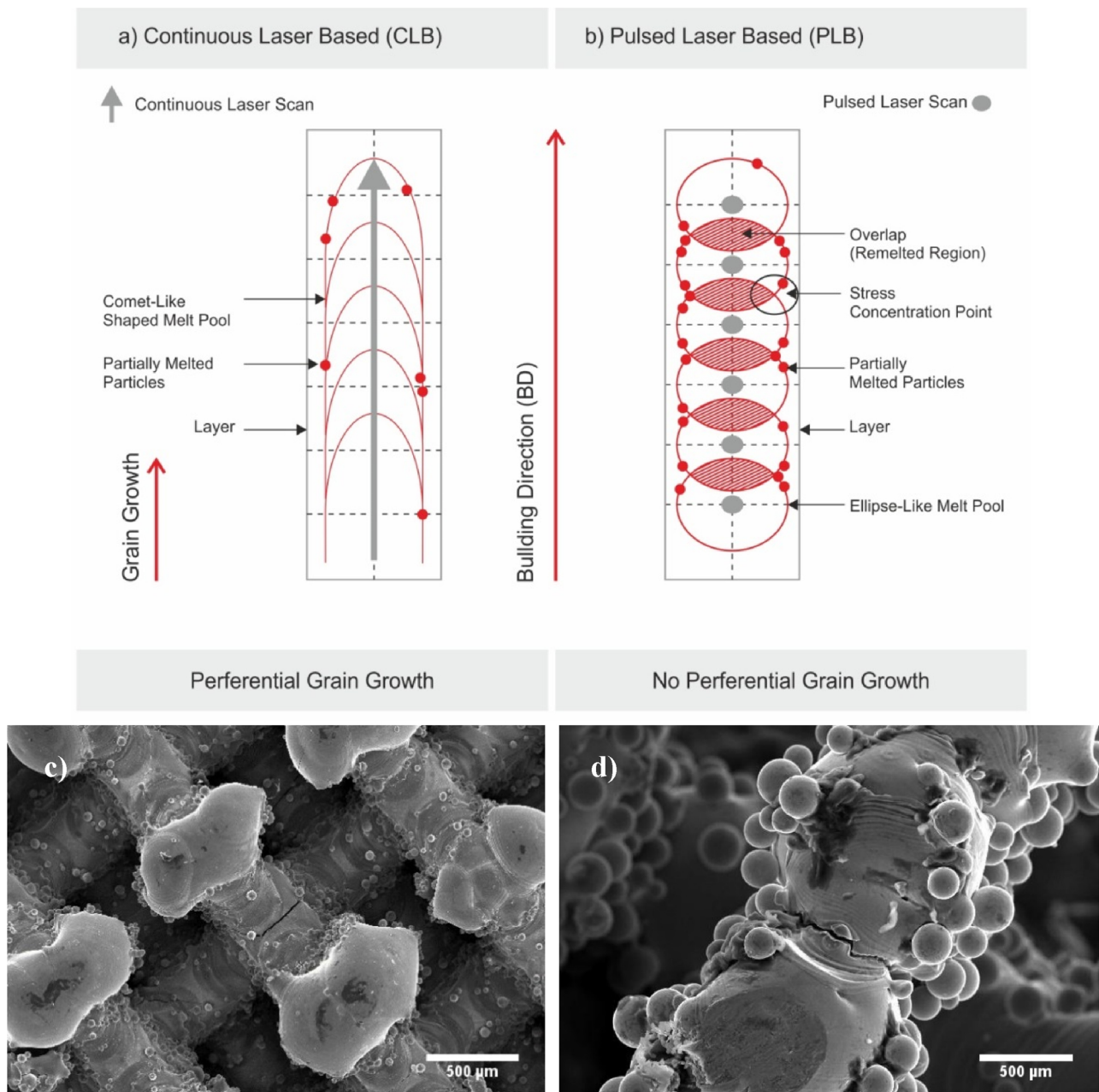


Fig. 15. A schematic illustration showing the different laser scanning methods including (a) CLB (b) PLB as well as the SEM micrographs showing the location of crack initiation for the (c) CLB and (d) PLB modes.

### Declaration of Competing Interest

The authors declare that they have no known competing financial interests or personal relationships that could have appeared to influence the work reported in this paper.

### References

- [1] B. Vandenbroucke, J.-P. Kruth, Selective laser melting of biocompatible metals for rapid manufacturing of medical parts, *Rapid Prototyp. J.* 13 (4) (2007) 196–203.
- [2] R. Wauthle, Industrialization of selective laser melting for the production of porous titanium and tantalum implants, (2014).
- [3] ISO / ASTM52900-52915, *Standard Terminology for Additive Manufacturing – General Principles – Terminology*, ASTM International, West Conshohocken, PA, 2015.
- [4] J.C. Chekotu, R. Groarke, K. O'Toole, D. Brabazon, Advances in Selective Laser Melting of Nitinol Shape Memory Alloy Part Production, 12(5) (2019) 809.
- [5] E. Hosseini, V.A. Popovich, A review of mechanical properties of additively manufactured Inconel 718, 30 (2019) 100877.
- [6] A.R. Nassar, E. Reutzel, Additive manufacturing of Ti-6Al-4V using a pulsed laser beam, 46(6) (2015) 2781–2789.
- [7] S. Huang, S.L. Sing, G. Looze, R. Wilson, W.Y. Yeong, Laser powder bed fusion of titanium-tantalum alloys: compositions and designs for biomedical applications, *J. Mech. Behav. Biomed. Mater.* 108 (2020) 103775.
- [8] S.L. Sing, S. Huang, W.Y. Yeong, Effect of solution heat treatment on microstructure and mechanical properties of laser powder bed fusion produced cobalt-28chromium-6molybdenum, *Mater. Sci. Eng. A* 769 (2020) 13851.
- [9] J.-P. Kruth, P. Mercelis, J. Van Vaerenbergh, L. Froyen and M. Rombouts, Binding mechanisms in selective laser sintering and selective laser melting, 11(1) (2005) 26–36.
- [10] L. Thijs, F. Verhaeghe, T. Craeghs, J. Van Humbeeck and J.-P. Kruth, A study of the microstructural evolution during selective laser melting of Ti-6Al-4V, 58(9) (2010) 3303–3312.
- [11] R. Stamp, P. Fox, W. O'Neill, E. Jones and C. Sutcliffe, The development of a scanning strategy for the manufacture of porous biomaterials by selective laser melting, 20(9) (2009) 1839.
- [12] C. Zhang, H. Zhu, Z. Hu, L. Zhang, X. J. M. S. Zeng, A comparative study on single-laser and multi-laser selective laser melting AlSi10Mg: defects, microstructure and mechanical properties, 746 (2019) 416–423.

- [13] H. Shipley, D. McDonnell, M. Culleton, R. Coull, R. Lupoi, G. O'Donnell, D. Trimble, Optimisation of process parameters to address fundamental challenges during selective laser melting of Ti-6Al-4V: A review, 128 (2018) 1-20.
- [14] L.W.X. Ding, S. Wang, Comparison Study of Numerical Analysis for Heat Transfer and Fluid Flow Under Two Different Laser Scan Pattern During Selective Laser Melting, (2016), pp. 10898-10907.
- [15] S. Ahmadi, R. Hedayati, R. A. K. Jain, Y. Li, S. Leeftang, A.A. Zadpoor, Effects of laser processing parameters on the mechanical properties, topology, and microstructure of additively manufactured porous metallic biomaterials: A vector-based approach, 134 (2017) 234-243.
- [16] E. Brandl, F. Palm, V. Michailov, B. Viehweger, C. Leyens, Mechanical properties of additive manufactured titanium (Ti-6Al-4V) blocks deposited by a solid-state laser and wire, 32(10) (2011) 4665-4675.
- [17] S. Kuriakose and M. Shunmugam, Characteristics of wire-electro discharge machined Ti6Al4V surface, 58(17-18) (2004) 2231-2237.
- [18] A.A. Antonsamy, Microstructure, Texture and Mechanical Property Evolution During Additive Manufacturing of Ti6Al4V Alloy for Aerospace Applications, The University of Manchester, United Kingdom, 2012.
- [19] K. Bundy, Biomaterials and the Chemical Environment of the Body, in Joint Replacement Technology, (2008), pp. 56-80.
- [20] C. Elias, J. Lima, R. Valiev and M. Meyers, Biomedical applications of titanium and its alloys, 60(3) (2008) 46-49.
- [21] R. Pederson, Microstructure and Phase Transformation of Ti-6Al-4V, Luleå tekniska universitet, 2002.
- [22] L. Yuan, S. Ding and C. Wen, Additive manufacturing technology for porous metal implant applications and triple minimal surface structures: A review. 4(1) (2019) 56-70.
- [23] B. Levine, A new era in porous metals: applications in orthopaedics. 10(9) (2008) 788-792.
- [24] X. Li, C. Wang, W. Zhang and Y. Li, Fabrication and compressive properties of Ti6Al4V implant with honeycomb-like structure for biomedical applications. 16(1) (2010) 44-49.
- [25] A.A. Zadpoor, Meta-biomaterials, *Biomater. Sci.* 8 (1) (2020) 18-38.
- [26] J. H. Lee, J. P. Singer and E. Thomas, Micro-/nanostructured mechanical meta-materials, 24(36) (2012) 4782-4810.
- [27] S. Ahmadi, R. Hedayati, Y. Li, K. Lietaert, N. Tümer, A. Fatemi, C.D. Rans, B. Pouran, H. Weinans, A.A. Zadpoor, Fatigue performance of additively manufactured meta-biomaterials: The effects of topology and material type, 65 (2018) 292-304.
- [28] B. Van Hooreweder, Y. Apers, K. Lietaert and J.-P. Kruth, Improving the fatigue performance of porous metallic biomaterials produced by Selective Laser Melting, 47 (2017) 93-202.
- [29] S. A. Yavari, S. Ahmadi, R. Wauthle, B. Pouran, J. Schrooten, H. Weinans, A.A. Zadpoor, Relationship between unit cell type and porosity and the fatigue behavior of selective laser melted meta-biomaterials, 43 (2015) 91-100.
- [30] S. A. Yavari, R. Wauthlé, J. van der Stok, A. Rienslag, M. Janssen, M. Mulier, A.A. Zadpoor, Fatigue behavior of porous biomaterials manufactured using selective laser melting, 33(8) (2013) 4849-4858.
- [31] S. M. Ahmadi, R. Kumar, E.V. Borisov, R. Petrov, S. Leeftang, Y. Li, N. Tümer, R. Huiyenga, C. Ayas, A.A. Zadpoor, V.A. Popovich, From microstructural design to surface engineering: A tailored approach for improving fatigue life of additively manufactured meta-biomaterials, 83 (2019) 153-166.
- [32] N. Loh and K. Sia, An overview of hot isostatic pressing, 30(1) (1992) 45-65.
- [33] S.M. Ahmadi, R.A.K. Jain, A.A. Zadpoor, C. Ayas, V.A. Popovich, Effects of heat treatment on microstructure and mechanical behaviour of additive manufactured porous Ti6Al4V, IOP Conference Series: Materials Science and Engineering 293 (2017) IOP Publishing.
- [34] R. Hedayati, S. Ahmadi, K. Lietaert, B. Pouran, Y. Li, H. Weinans, A.A. Zadpoor, Isolated and modulated effects of topology and material type on the mechanical properties of additively manufactured porous biomaterials. 79 (2018) 254-263.
- [35] C. Leyens, M. Peters, Titanium and Titanium Alloys: Fundamentals and Applications, John Wiley & Sons, 2003.
- [36] M. Niinomi, Mechanical properties of biomedical titanium alloys, 243 (1-2) (1998) 231-236.
- [37] S. Li, H. Xiao, K. Liu, W. Xiao, Y. Li, X. Han, J. Mazumder, L. Song, Melt-pool motion, temperature variation and dendritic morphology of Inconel 718 during pulsed-and continuous-wave laser additive manufacturing: A comparative study, 119 (2017) 351-360.
- [38] G. Ravi, C. Qiu and M. Attallah, Microstructural control in a Ti-based alloy by changing laser processing mode and power during direct laser deposition, 179 (2016) 104-108.
- [39] S. Ghouse, S. Babu, R. J. Van Arkel, K. Nai, P. A. Hooper, J. Jeffers, et al., The influence of laser parameters and scanning strategies on the mechanical properties of a stochastic porous material, 131 (2017) 498-508.
- [40] C. Biffi, J. Fiochi, P. Bassani and A. Tuissi, Continuous wave vs pulsed wave laser emission in selective laser melting of AlSi10Mg parts with industrial optimized process parameters: microstructure and mechanical behaviour, 24 (2018) 639-646.
- [41] L. Caprio, A.G. Demir, B. Previtali, Atlanta, GA, USA, October 22-26, Comparative Study Between CW and PW Emissions in Selective Laser Melting, (2017), p. 1304.
- [42] J. Kim, S. Ji, Y.-S. Yun, J. Yeo, A Review: Melt Pool Analysis for Selective Laser Melting with Continuous Wave and Pulse Width Modulated Lasers, 27(6) (2018) 113-119.
- [43] A. G. Demir, P. Colombo and B. Previtali, From pulsed to continuous wave emission in SLM with contemporary fiber laser sources: effect of temporal and spatial pulse overlap in part quality, 91(5-8) (2017) 2701-2714.
- [44] C. Qiu, C. Panwisawas, M. Ward, H. C. Basoalto, J. W. Brooks and M. Attallah, On the role of melt flow into the surface structure and porosity development during selective laser melting, 96 (2015) 72-79.
- [45] S. Ahmadi, G. Campoli, S. A. Yavari, B. Sajadi, R. Wauthlé, J. Schrooten, A.A. Zadpoor, Mechanical behavior of regular open-cell porous biomaterials made of diamond lattice unit cells, 34 (2014) 106-115.
- [46] C. Cayron, ARPGE: a computer program to automatically reconstruct the parent grains from electron backscatter diffraction data, 40(6) (2007) 1183-1188.
- [47] ISO 13314, (E)(2011) Mechanical Testing of Metals—ductility Testing—compression Test for Porous and Cellular Metals, 13314(13314) (2011), pp. 1-7.
- [48] S. Deviant, The Practically Cheating Statistics Handbook, Lulu. com, 2011.
- [49] L.J. Gibson, M.F. Ashby, Cellular Solids: Structure and Properties, Cambridge university press, 1999.
- [50] A. Zargarian, M. Esfahanian, J. Kadhodapour, S. Ziaei-Rad., Numerical simulation of the fatigue behavior of additive manufactured titanium porous lattice structures, 60 (2016), 339-347.
- [51] P. Collins, D. Brice, P. Samimi, I. Ghamarian and H. Fraser, Microstructural control of additively manufactured metallic materials, 46 (2016) 63-91.
- [52] A. Basak and S. Das, Epitaxy and microstructure evolution in metal additive manufacturing. 46 (2016) 125-149.
- [53] E. Onal, A. Medvedev, M. Leeftang, A. Molotnikov and A.A. Zadpoor, Novel microstructural features of selective laser melted lattice struts fabricated with single point exposure scanning. 29 (2019) 100785.
- [54] X. Ding, L. Wang and S. Wang, Comparison study of numerical analysis for heat transfer and fluid flow under two different laser scan pattern during selective laser melting, 127(22) (2016) 10898-10907.
- [55] S. Malinov, Z. Guo, W. Sha, A. Wilson, Differential scanning calorimetry study and computer modeling of  $\beta \Rightarrow \alpha$  phase transformation in a Ti-6Al-4V alloy, 32(4) (2001) 879-887.
- [56] G. Kasperovich and J. Hausmann, Improvement of fatigue resistance and ductility of TiAl6V4 processed by selective laser melting, 220 (2015) 202-214.
- [57] R. Wauthle, B. Vrancken, B. Beynaerts, K. Jorissen, J. Schrooten, J.-P. Kruth, Effects of build orientation and heat treatment on the microstructure and mechanical properties of selective laser melted Ti6Al4V lattice structures, 5 (2015) 77-84.
- [58] B. Baufeld, E. Brandl and O. Van der Biest, Wire based additive layer manufacturing: Comparison of microstructure and mechanical properties of Ti-6Al-4V components fabricated by laser-beam deposition and shaped metal deposition, 211(6) (2011) 1146-1158.
- [59] R. Nalla, J. Campbell, R. J. F. Ritchie, Effects of microstructure on mixed-mode, high-cycle fatigue crack-growth thresholds in Ti-6Al-4V alloy, 25(6) (2002) 587-606.
- [60] Y. Zhai, D. A. Lados, E. J. Brown and G. Vigilante, Fatigue crack growth behavior and microstructural mechanisms in Ti-6Al-4V manufactured by laser engineered net shaping, 93 (2016) 51-63.
- [61] T. Vilaro, C. Colin, J. Bartout, As-fabricated and heat-treated microstructures of the Ti-6Al-4V alloy processed by selective laser melting, 42(10) (2011) 3190-3199.
- [62] C. Chen, Y. Xie, X. Yan, S. Yin, H. Fukunuma, R. Huang, Effect of hot isostatic pressing (HIP) on microstructure and mechanical properties of Ti6Al4V alloy fabricated by cold spray additive manufacturing, 27 (2019) 595-605.
- [63] B. Vrancken, L. Thijs, J.-P. Kruth, J. Van Humbeeck, Heat treatment of Ti6Al4V produced by Selective Laser Melting: Microstructure and mechanical properties. 541 (2012) 177-185.
- [64] S. L. Sing, F. E. Wiria, W. Yeong, Selective laser melting of lattice structures: A statistical approach to manufacturability and mechanical behavior, 49 (2018) 170-180.
- [65] N. T. Aboulkhair, N. M. Everitt, I. Ashcroft and C. Tuck, Reducing porosity in AlSi10Mg parts processed by selective laser melting, 1 (2014) 77-86.
- [66] Z. Dong, Y. Liu, W. Li and J. Liang, Orientation dependency for microstructure, geometric accuracy and mechanical properties of selective laser melting AlSi10Mg lattices, 791 (2019) 490-500.
- [67] M. Smith, Z. Guan and W. Cantwell, Finite element modelling of the compressive response of lattice structures manufactured using the selective laser melting technique, 67 (2013) 28-41.
- [68] L.J. Gibson, M.F. Ashby, Cellular Solids, Structure and Properties, 2nd ed., Cambridge University Press, UK, 1997.
- [69] W. Yu, S.L. Sing, C.K. Chua, X. Tian, Influence of re-melting on surface roughness and porosity of AlSi10Mg parts fabricated by selective laser melting, J. Alloys. Compd. 792 (2019) 574-581.
- [70] J. Guan, Y. Jiang, X. Zhang, X. Chong, Microstructural evolution and EBSD analysis of AlSi10Mg alloy fabricated by selective laser remelting, Mater. Charact. 161 (2020) 110079.
- [71] B. Song, S. Dong, B. Zhang, H. Liao, C. Coddet, Effects of processing parameters on microstructure and mechanical property of selective laser melted Ti6Al4V, Mater. Des. 1 (March 35) (2012) 120-125.
- [72] R. Chou, J. Milligan, M. Paliwal, M. Brochu, Additive manufacturing of Al-12Si alloy via pulsed selective laser melting, Jom 1 (March (3)) (2015) 590-596 67.